

A Novel Environment Object Modeling Method for Vehicular ISAC Scenarios

Hanyuan Jiang*, Yuxiang Zhang*, Yameng Liu*, Jianhua Zhang*, Lei Tian*, Tao Jiang†

*State Key Lab of Networking and Switching Technology, Beijing University of Posts and Telecommunications, Beijing, China

†China Mobile Research Institution, Beijing, China

*{jianghy, zhangyx, liuym, tianlbupt, jhzhang}@bupt.edu.cn

†jiangtao@chinamobile.com

Abstract—Integrated Sensing and Communication (ISAC), as a fundamental technology of 6G, empowers Vehicle-to-Everything (V2X) systems with enhanced sensing capabilities. One of its promising applications is the reliance on constructed maps for vehicle positioning. Traditional positioning methods primarily rely on Line-of-Sight (LOS), but in urban vehicular scenarios, obstructions often result in predominantly Non-Line-of-Sight (NLOS) conditions. Existing researches indicate that NLOS paths, characterized by one-bounce reflection on building wall with determined delay and angle, can support sensing and positioning. However, experimental validation remains insufficient. To address this gap, channel measurements are conducted in an urban street to explore the existence of strong reflected paths in the presence of a vehicle target. The results show significant power contribution from NLOS paths, with large Environmental Objects (EOs) playing a key role in shaping NLOS propagation. Then, a novel model for EO reflection is proposed to extend the Geometry-Based Stochastic Model (GBSM) for ISAC channel standardization. Simulation results validate the model’s ability to capture EO’s power and position characteristics, showing that higher EO-reflected power and closer distance to Rx reduce Delay Spread (DS), which is more favorable for positioning. This model provides theoretical guidance and empirical support for ISAC positioning algorithms and system design in vehicular scenarios.

Index Terms—6G, ISAC, Channel measurement, V2X, NLOS, Environment Object.

Integrated Sensing and Communication (ISAC) is emerging as a fundamental technology to realize ubiquitous sensing and support digital twins within 6G networks [1]. Unlike conventional systems that are typically limited to either communication or sensing, ISAC combines both functions into a unified framework. This allows base stations and terminals to perform communication tasks while concurrently sensing the environment [2]. Vehicle-to-Everything (V2X) serves as a typical application scenario for ISAC, playing a significant role in enabling autonomous driving [3], [4]. Notably, vehicle positioning is one of the key functions, relying on the acquisition of environmental information for map construction, and using algorithms to accurately determine the vehicle’s location [5].

Traditional positioning algorithms, such as TOA (Time of Arrival) and TDOA (Time Difference of Arrival), are suitable for ideal LOS (Line of Sight) condition [6], [7]. However, in urban vehicular scenarios, the presence of obstacles such as buildings and trees adds complexity to the environment,

resulting in significant multipaths effects that degrade positioning accuracy [8]. To address this challenge, [9] proposes using NLOS paths that undergo one-bounce reflection and leverages bidirectional estimation of the Angle of Arrival (AOA) and TOA. In addition, [10] finds through ray-tracing simulations that NLOS positioning primarily relies on fixed and regular scatterers in the environment, such as walls. These scatterers are referred to as environment objects (EOs) while other multiple-bounce scattering paths should be discarded as much as possible.

However, most of these findings are based on theoretical analysis and simulation studies. They have not been validated by measurements to confirm whether urban vehicular scenarios contain EOs that can reflect one-bounce strong power NLOS paths for positioning. Furthermore, [11] discusses the 3GPP’s latest need for modeling EO to better characterize the propagation characteristics of ISAC channel in vehicular scenarios. Yet, this theory remains unsupported by experimental validation.

Therefore, this paper aims to address the aforementioned gaps by conducting bi-static measurements in an urban street environment, with a vehicle as sensing target at 26 GHz. The results reveal that the power of NLOS paths is sufficiently strong for sensing, primarily influenced by large EOs such as wall and metal fence. To quantify this impact, K_{EO} -factor is introduced to describe the proportional relationship between NLOS paths and EO-reflected paths. Furthermore, a novel EO reflection model is proposed based on ground reflection in Geometry-Based Stochastic Model (GBSM), offering a more accurate representation under NLOS condition in ISAC channel. Simulation results validate this model’s effectiveness in capturing both EO power and position characteristics, as evidenced by shifts in the Cumulative Distribution Function (CDF) of Delay Spread (DS).

The remainder of the paper is organized as follows. Section II describes the measurement system and scheme. Section III presents the measurement results and conducts a quantitative analysis of the power contributions from different scatterers in the ISAC channel. Section IV focuses on the modeling of EO especially in NLOS condition, providing expressions based on ground reflection, along with the simulation results on DS under different power proportions and EO positions.

Section V provides the conclusion of this study.

I. MEASUREMENTS DESCRIPTION

A. Measurement System

In this measurement experiment, the Transmitter (Tx) utilizes a vector signal generator to generate a PN code sequence with a length of 1022 bits. The generated signal is then modulated to 26 GHz using binary phase shift keying and transmitted via a lens antenna, which provides excellent directivity and high gain, ensuring that more energy is directed toward the target. At the Receiver (Rx), a spectrum analyzer is used to capture and record the received signal. To ensure sufficient system gain, a low-noise amplifier is used at the receiver to amplify the signal [12]. Fig. 1 illustrates the structure of the measurement system. The specific configuration is detailed in Table. I.

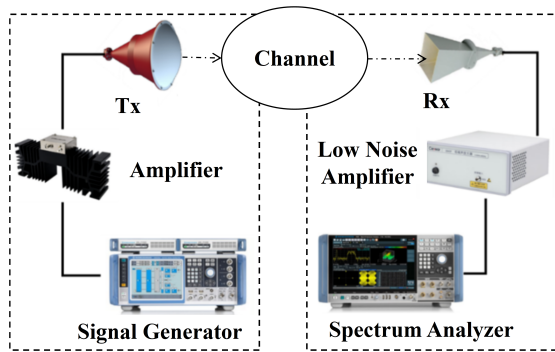


Fig. 1: Measurement system diagram.

TABLE I: Measurement System Configuration

Parameters	Value/Type
Center frequency (GHz)	26
Bandwidth (MHz)	600
PN sequence	1022
Horn antenna azimuth HPBW (deg)	8
Lens Horn Antenna azimuth HPBW (deg)	4.75
Height of Tx/Rx Antenna (m)	1.6
Antenna polarization	V-to-V

B. Measurement Scheme

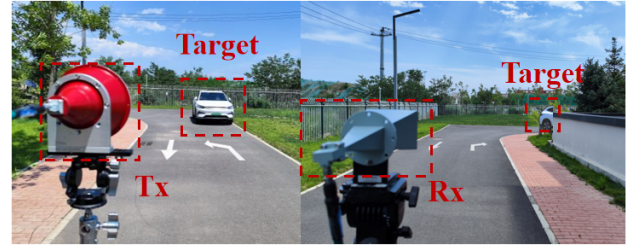
As depicted in Fig. 2, a Bi-static ISAC channel measurement campaign is conducted along an urban L-shaped street. The selected environment facilitates clear scatterers identification including tall building wall, dense metal fence, lampposts, and vegetation. The Tx, equipped with a lens antenna, is positioned on the west side of the street transmitting eastward. A horn antenna on the north side faces south at a 0° angle. The horn antenna is rotated both clockwise and counterclockwise, collecting data every 5° across a range of $\pm 90^\circ$, resulting in a total of 36 receiving angles. The absence of a LOS path between Tx and Rx is noted, obstructed by a tall building.

Two cases are designed to investigate the sensing of target by Rx in bi-static mode. Initially, a $4.2m \times 1.7m \times 1.6m$

vehicle is positioned at a 45° angle in the corner of the street, facing the Tx (Case 1, Fig.2(a)). In this scenario, the vehicle is aligned with the Tx, establishing a clear LOS path. This setup simulates a typical turning scenario, where the vehicle is in motion and about to change direction. In Case 2 (Fig.2(b)), the vehicle is moved to the left side of the east-west street, facing west. In this situation, there is no direct alignment with the Tx, and there is also no clear LOS path to the Rx. This setup represents a scenario where the vehicle is about to complete its turn at the intersection.



(a) Case1 scenario



(b) Case2 scenario

Fig. 2: The measurement campaign

II. MEASUREMENT RESULTS AND ANALYSIS

To visualize the distribution of multipath components (MPCs) across delay, spatial, and power domains, Fig. 3 presents the Power-Angular Delay Profiles (PADPs) under various cases, along with the analysis of potential propagation paths. In the environment, the PADP clearly distinguishes various scatterers, such as the metal fence, wall, and lampposts, highlighting their individual contributions to the MPCs. When the vehicle is introduced into the environment, one-bounce reflection from the vehicle (label A) becomes clearly noticeable in Case 1. However, it is relatively weaker in Case 2 due to the absence of a distinct LOS path. By comparing the PADP of Case 1 and Case 2 with the baseline environment, the observed changes reveal the MPCs influenced by the vehicle and reflected from the surrounding scatterers, labeled as B, C and D. These MPCs that interact with the vehicle and are finally received can be defined as the target channel.

Subsequently, a quantitative analysis on the power proportion of different paths in target channel is conducted to further investigate which scatterers matter in the vehicular scenario. First, we accurately measure the size of the environment, calculating the distances and angle ranges that the signal

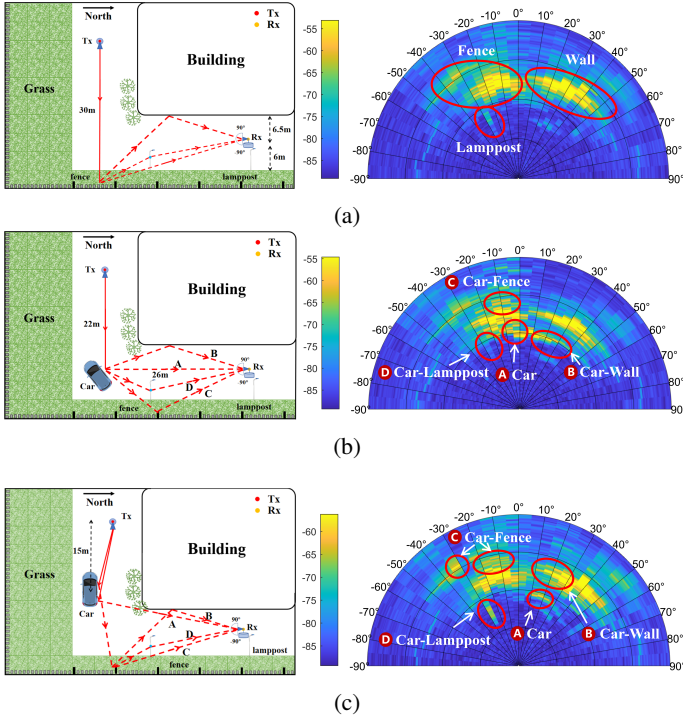


Fig. 3: The analysis of possible paths and result of PADP for different cases are as follows: (a) Environment. (b) Case1. (c) Case2.

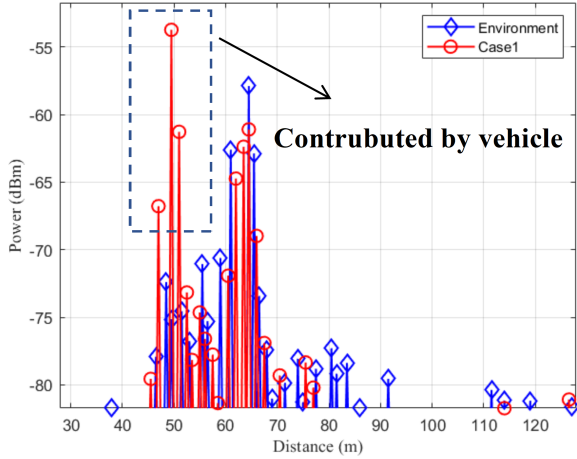


Fig. 4: Illustration of the comparison of MPCs at Rx with 5° angle between the environment and Case 1. The additional red lines at the 48m position indicate the effective MPCs contributed by the vehicle target.

propagates from Tx through various scatterers to the receiver, ensuring the precise identification of the corresponding MPCs. By comparing the Power Delay Profiles (PDP) of the environment, Case 1, and Case 2 at the same angles, MPCs attributed by the vehicle are identified as shown in Fig. 4. Moreover, measurement data reveal that wall and fence, as relatively regular scatterers, exhibit strong energy at receiver angles when facing them at specific incident and reflection

angles, which suggests the adherence to specular reflection mechanism. Therefore, the MPCs contributed by the target and then reflected by different scatterers can be separated at all Rx angles.

Then, the power contribution $PP_{scatterer}$ of each scatterer to the target channel is calculated, as shown in (1). In this equation, $P_{scatterer}$ represents the total power from a specific scatterer across N measured angles, which is 36 in this measurement. While P_{tar} denotes the total power of the target channel across all angles, which includes the sum of power contributions from all scatterers. This method quantifies the relative contribution of each scatterer to the overall target channel power, helping to identify which scatterers have the most significant impact. Table.II and Table.III summarize the power proportions of different paths in target channel.

$$PP_{scatterer} = \frac{P_{scatterer}}{P_{tar}} = \frac{\sum_{i=1}^N P_{scatterer,i}}{\sum_{i=1}^N P_{tar,i}} \quad (1)$$

TABLE II: Power proportion of different paths in target channel for Case 1

Path	Contributed by	Propagation	Distance/Angle	Power proportion
A	Vehicle	LOS-LOS	47m~51m ($-5^\circ \sim 5^\circ$)	50.5%
B	Vehicle-Wall	LOS-NLOS	50m~53m ($15^\circ \sim 55^\circ$)	9.7%
C	Vehicle-Fence	LOS-NLOS	52m~58m ($-55^\circ \sim -15^\circ$)	34.5%
D	Vehicle-Lamppost	LOS-NLOS	49m~50m ($-30^\circ \sim -25^\circ$)	5.3%

TABLE III: Power proportion of different paths in target channel for Case 2

Path	Contributed by	Propagation	Distance/Angle	Power proportion
A	Vehicle	LOS-LOS	45m~48m ($-5^\circ \sim 5^\circ$)	17.9%
B	Vehicle-Fence-Wall	LOS-NLOS	60m~66m ($15^\circ \sim 55^\circ$)	61.3%
C	Vehicle-Fence	LOS-NLOS	52m~58m ($-55^\circ \sim -5^\circ$)	8.4%
D	Vehicle-Fence-lamppost	LOS-NLOS	49m~50m ($-30^\circ \sim -25^\circ$)	12.4%

The measurement results indicate that when a vehicle target is introduced, environmental scatterers impact the target channel to varying degrees. Small scatterers like lampposts contribute relatively little power, around 12% in Case 2 and only 5% in Case 1. In contrast, large regular scatterers such as wall and metal fence significantly affect the target channel. In Case 1, besides direct reflection from vehicle, the metal fence and wall contribute about 45% of the power, while in Case 2, due to the absence of LOS paths, they contribute approximately up to 70%. These scatterers can be defined as EOs, which play a critical role in the target channel. As a result, the power from EOs is sufficiently strong to be leveraged for NLOS-assisted sensing.

$$H_{u,s}^{\text{NLOS}}(\tau, t) = \sqrt{K_{EO}} \cdot \sum_{k=1}^K H_{u,s,k}^{\text{EO}}(t) \delta(\tau - \tau_{EO,k}) + \sqrt{1 - K_{EO}} \cdot \sum_{n=1}^N H_{u,s,n}^{\text{NLOS}}(t) \delta(\tau - \tau_n) \quad (3)$$

$$H_{u,s}^{\text{EO}}(t, \tau) = \begin{bmatrix} F_{rx,u,\theta}(\theta_{EO,ZOA}, \phi_{EO,AOA}) \\ F_{rx,u,\phi}(\theta_{EO,ZOA}, \phi_{EO,AOA}) \end{bmatrix}^T \cdot \begin{bmatrix} R_{\parallel}^{\text{EO}} & 0 \\ 0 & -R_{\perp}^{\text{EO}} \end{bmatrix} \cdot \begin{bmatrix} F_{tx,s,\theta}(\theta_{EO,ZOD}, \phi_{EO,AOD}) \\ F_{tx,s,\phi}(\theta_{EO,ZOD}, \phi_{EO,AOD}) \end{bmatrix} \\ \cdot \exp\left(-j2\pi \frac{d_{EO}}{\lambda_0}\right) \exp\left(j2\pi \frac{\hat{r}_{rx,EO}^T \cdot \mathbf{d}_{rx,u}}{\lambda_0}\right) \cdot \exp\left(j2\pi \frac{\hat{r}_{tx,EO}^T \cdot \mathbf{d}_{tx,s}}{\lambda_0}\right) \\ \cdot \exp\left(j2\pi \frac{\hat{r}_{tx,EO}^T \cdot \mathbf{v}_{tx}}{\lambda_0} t\right) \cdot \exp\left(j2\pi \frac{\hat{r}_{rx,EO}^T \cdot \mathbf{v}_{rx}}{\lambda_0} t\right) \quad (4)$$

$$\tau_{EO} = \frac{d_{EO}}{c} = \frac{\sqrt{(h_{tx} - h_{rx})^2 + (d_{tx} + d_{rx})^2 + d_{2D}^2 - (d_{tx} - d_{rx})^2}}{c} \quad (5)$$

III. MODELING OF ENVIRONMENT OBJECT

A. EO modeling in GBSM

The previous section reveals that, in urban vehicular ISAC scenarios, a significant portion of the power in target channel originates from EOs, making it essential to model these components for positioning. In the bi-static sensing mode, due to the presence of target, the channel is divided into Tx-target and target-Rx components, which exhibit the same characteristics due to channel reciprocity, as illustrated in Fig.5. Therefore, This section focuses on modeling the EO within target-Rx channel, assuming the vehicle acts as a transmitter in target channel. What's more, similar to the ground reflection model in GBSM [13], EOs can be treated as specular reflection surfaces and are typically considered strong paths under NLOS conditions, as indicated by the previous measurement results.

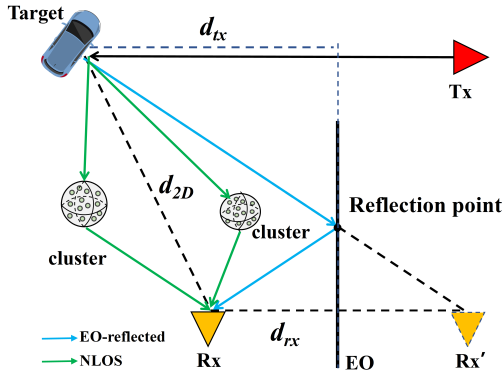


Fig. 5: Illusion of EO reflection.

To quantify the power contribution of the EO-reflected path, the K_{EO} -factor is proposed, as defined in (2). Here, P_{EO} and P_{NLOS} denote the total power of EO-reflected paths and the overall NLOS power in the environment, respectively.

This parameter serves as a measure of the presence and influence of EOs within the environment. Specifically, when $K_{EO} = 0$, it indicates the absence of significant EOs, whereas a higher K_{EO} value suggests that the majority of NLOS power originates from EO-reflected paths.

$$K_{EO} = \frac{P_{EO}}{P_{NLOS}}, \quad K_{EO} \in [0, 1] \quad (2)$$

When considering EO-reflected path in NLOS propagation, the total channel impulse response (CIR) under NLOS condition is expressed in (3). The total NLOS channel response $H_{u,s}^{\text{NLOS}}$ is the summation of the EO-reflected paths and other NLOS paths, where K and N represent the total number of EO-reflected paths and other NLOS paths, respectively. The CIR for the original NLOS paths $H_{u,s,n}^{\text{NLOS}}$ is generated based on the steps described in [13]. For EO-reflected path within a 3D-MIMO system [14], the CIR is defined by (4), where

- $F_{rx,u,\theta}$ and $F_{rx,u,\phi}$ are the field patterns of receive antenna element u the direction of the spherical basis vectors, $\hat{\theta}$ and $\hat{\phi}$ respectively.
- $F_{tx,s,\theta}$ and $F_{tx,s,\phi}$ are the field patterns of transmit antenna element s in the direction of the spherical basis vectors, $\hat{\theta}$ and $\hat{\phi}$ respectively.
- $\theta_{EO,ZOA}$ and $\phi_{EO,AOA}$ are the zenith and azimuth angle of arrival after interacting with the EO.
- $\theta_{EO,ZOD}$ and $\phi_{EO,AOD}$ are the zenith and azimuth angle of departure after interacting with the EO.
- $R_{\parallel}^{\text{EO}}$ and R_{\perp}^{EO} represent the reflection coefficients for parallel and perpendicular polarization, which vary with different materials and surfaces of EO.
- d_{EO} represents the propagation distance of EO-reflected path.
- λ_0 is the wavelength of the carrier frequency.
- $\hat{r}_{tx,EO}, \hat{r}_{rx,EO}$ indicate the unit vectors from the Tx or Rx to the EO, respectively.

- $\mathbf{d}_{tx,u}, \mathbf{d}_{rx,s}$ indicate the location vectors of the transmitter and receiver antennas.
- $\mathbf{v}_{tx}, \mathbf{v}_{rx}$ indicate the velocity vectors of transmitter and receiver.

Since NLOS-assisted positioning primarily relies on one-bounce reflected paths, while multiple-bounce paths are treated as noise that affect positioning accuracy, the EO modeling above mainly focuses on one-bounce reflections. Therefore, the position of EO can be determined by defining the horizontal distances d_{tx} and d_{rx} from the Tx and Rx to EO, respectively. Consequently, the delay, angles, and other parameters can be derived based on geometric relationships and theoretical formula, as shown in (5), where h_{tx} and h_{rx} are the height of Tx and Rx respectively. d_{2D} indicates the horizon distance between Tx and Rx.

B. Numerical Analysis

To validate the impact of EO modeling on the channel, we conduct simulations of real-world scenarios and compare the results with measurement data. Based on the formulas, the target-Rx channel in Urban Microcell(Umi) scenario with a single EO as reflecting wall surface can be simulated. The configuration parameters are shown in Table IV, with $d_{tx} = d_{rx} = 6.5$ m and $K_{EO} = 0.5$, which is the same deployment as the measurement described in section II.

TABLE IV: Simulation Configuration

Parameters	Value/Type
Scenario	Umi urban street
Link condition	NLOS
Center frequency (GHz)	26
Bandwidth (MHz)	600
Number of Tx/Rx	1
Coordinates of Tx/Rx (m)	(0,0,1.6)/(0,26,1.6)
Type of Tx/Rx antenna	Horn

Following simulation configuration described above, the PDP of target-Rx channel is plotted, as shown in Fig. 6. It can be observed that a distinct strong path appears at delay of 97 ns, which closely aligns with the absolute delay of 99 ns for the path reflected from target to the wall and then to Rx in the actual measurement scenario. The remaining MPCs describe the NLOS paths that reflected from other surrounding scatterers in the environment.

Since the delay spread (DS) reflects the multipath effects of the channel [15], a smaller DS indicates more concentrated energy, which is beneficial for improving positioning accuracy. Therefore, to further investigate the impact of introducing an EO on channel delay characteristics, simulations are conducted. Firstly, the K_{EO} -factor is varied to simulate different power contributions from the EO-reflected path, enabling the observation of changes in the CDF of DS under varying reflection intensities. Furthermore, the power contribution in the NLOS environment is kept constant, while

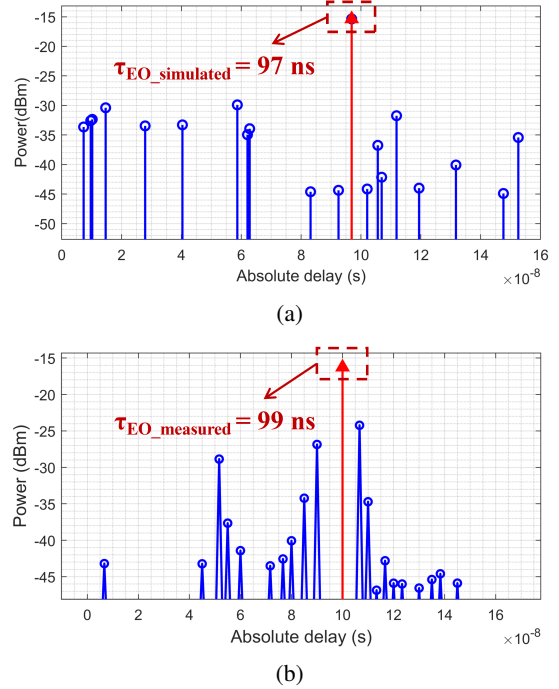


Fig. 6: Simulated PDP result (a) is based on the configuration parameters in TableIV, which is corresponding to the measurement result (b).

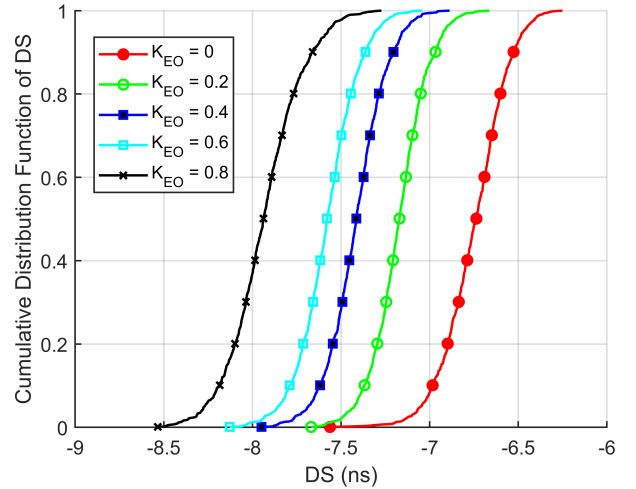


Fig. 7: CDF of DS under different K_{EO} values.

the distance between the EO and Rx is adjusted to examine how the position of EOs affects the CDF of DS.

The simulation results, as shown in Fig. 7 and 8, demonstrate that when the EO remains in the fixed position but the reflection power increases, the average DS decreases. This suggests that as more energy is focused on the EO-reflected path, the impact of other MPCs become smaller, which is more favorable for target sensing and positioning. Conversely, when the distance between the EO and the transmitter increases while keeping the power contribution

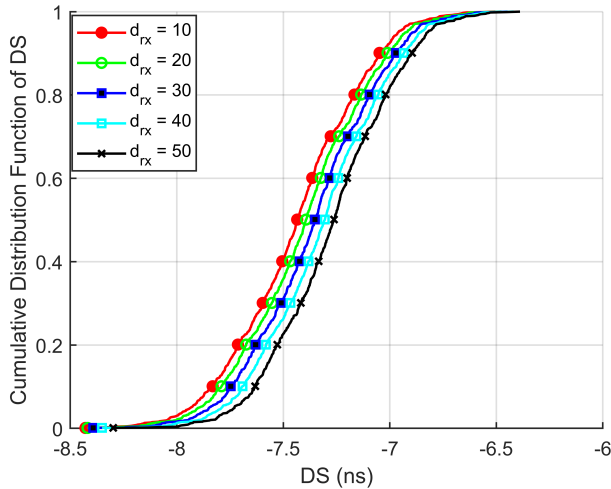


Fig. 8: CDF of DS under different d_{rx} values.

constant, the average DS increases. This implies that as the EO moves farther from the Rx, its influence on the channel weakens, leading to a more dispersed signal and indicating a lack of EOs in the environment that can assist in positioning. These findings highlight the critical role of the EO's reflection strength and location in influencing the target's sensing and positioning capabilities within the ISAC channel.

IV. CONCLUSION

This paper presents channel measurements in an urban vehicular scenario, emphasizing the notable power contributions reflected from large regular EOs in the target channel, which are favorable for sensing and positioning. An EO reflection model based on ground reflection in GBSM is introduced and validated through simulations, effectively capturing both EO power and position characteristics. These findings provide valuable insights for ISAC channel modeling and simulation in vehicular scenarios. Future research should focus on developing advanced algorithms and model designs to better leverage EO characteristics, further enhancing positioning and sensing performance.

ACKNOWLEDGMENT

This research is supported by National Key R&D Program of China (2023YFB2904802), Young Scientists Fund of the National Natural Science Foundation of China (62201087), The National Natural Science Foundation of China (U21B2014), Guangdong Major Project of Basic and Applied Basic Research (2023B0303000001), Key Program of Beijing Municipal Natural Science Foundation (L243002), and Beijing University of Posts and Telecommunications-China Mobile Research Institute Joint Innovation Center.

REFERENCES

[1] G. Liu, Y. Huang, N. Li, J. Dong, J. Jin, Q. Wang, and N. Li, "Vision, requirements and network architecture of 6G mobile network beyond 2030," *China Communications*, vol. 17, no. 9, pp. 92–104, 2020.

[2] J. Zhang, J. Lin, P. Tang, Y. Zhang, H. Xu, T. Gao, H. Miao, Z. Chai, Z. Zhou, Y. Li *et al.*, "Channel measurement, modeling, and simulation for 6G: A survey and tutorial," *arXiv preprint arXiv:2305.16616*, 2023.

[3] X. Cheng, D. Duan, S. Gao, and L. Yang, "Integrated sensing and communications (ISAC) for vehicular communication networks (VCN)," *IEEE Internet of Things Journal*, vol. 9, no. 23, pp. 23 441–23 451, 2022.

[4] Y. Zhong, T. Bi, J. Wang, J. Zeng, Y. Huang, T. Jiang, Q. Wu, and S. Wu, "Empowering the V2X network by integrated sensing and communications: Background, design, advances, and opportunities," *IEEE Network*, vol. 36, no. 4, pp. 54–60, 2022.

[5] G. T. SA, "Feasibility Study on Integrated Sensing and Communication," 3rd Generation Partnership Project, Tech. Rep. 22.837, 2024. [Online]. Available: <https://portal.3gpp.org/desktopmodules/Specifications/\protect\@normalcr\relaxSpecificationDetails.aspx?specificationId=4044>

[6] S. Kuutti, S. Fallah, K. Katsaros, M. Dianati, F. Mccullough, and A. Mouzakitis, "A survey of the state-of-the-art localization techniques and their potentials for autonomous vehicle applications," *IEEE Internet of Things Journal*, vol. 5, no. 2, pp. 829–846, 2018.

[7] I. Guvenc and C.-C. Chong, "A survey on TOA based wireless localization and NLOS mitigation techniques," *IEEE Communications Surveys & Tutorials*, vol. 11, no. 3, pp. 107–124, 2009.

[8] Q. Bader, S. Saleh, M. Elhabiby, and A. Noureldin, "NLoS detection for enhanced 5G mmWave-based positioning for vehicular iot applications," in *GLOBECOM 2022-2022 IEEE Global Communications Conference*. IEEE, 2022, pp. 5643–5648.

[9] S. Al-Jazzar and J. Caffery, "ML and Bayesian TOA location estimators for NLOS environments," in *Proceedings IEEE 56th vehicular technology conference*, vol. 2. IEEE, 2002, pp. 1178–1181.

[10] J. Chen, Z. Zhu, C. Qiu, P. Wu, S. Guo, G. Cui, and X. Yang, "LOS and NLOS Targets Localization in an L-Shaped Corner," in *IGARSS 2024-2024 IEEE International Geoscience and Remote Sensing Symposium*. IEEE, 2024, pp. 10 487–10 490.

[11] Y. Zhang, J. Zhang, Y. Pei, Y. Liu, and T. Jiang, "Latest progress for 3GPP ISAC channel modeling standardization," *Science China(Information Sciences)*, vol. 67, no. 11, pp. 357–358, 2024.

[12] J. Zhang, Y. Zhang, Y. Yu, R. Xu, Q. Zheng, and P. Zhang, "3-D MIMO: How much does it meet our expectations observed from channel measurements?" *IEEE Journal on Selected Areas in Communications*, vol. 35, no. 8, pp. 1887–1903, 2017.

[13] 3GPP, "Study on Channel Model for Frequencies from 0.5 to 100 GHz," 3rd Generation Partnership Project, Tech. Rep. 38.901, 2019. [Online]. Available: <https://www.3gpp.org/DynaReport/38901.htm>

[14] J. Zhang, C. Pan, F. Pei, G. Liu, and X. Cheng, "Three-dimensional fading channel models: A survey of elevation angle research," *IEEE communications magazine*, vol. 52, no. 6, pp. 218–226, 2014.

[15] T. Jiang, J. Zhang, P. Tang, L. Tian, Y. Zheng, J. Dou, H. Asplund, L. Raschkowski, R. D'Errico, and T. Jämsä, "3GPP standardized 5G channel model for IIoT scenarios: A survey," *IEEE Internet of Things Journal*, vol. 8, no. 11, pp. 8799–8815, 2021.